# Supporting Information for

# Metal organic framework-derived porous $Fe_2N$ nanocubes by rapid nitridation for highly efficient photocatalytic hydrogen evolution

Zhixing Cheng†§, Siqi Liu†§, Ali Saad†§, Samira Adimi†§, Haichuan Guo†§, Tiju Thomas*‡, and Minghui Yang*†§

E-mail: myang@nimte.ac.cn, liusiqi@nimte.ac.cn, tijuthomas@iitm.ac.in

† Ningbo Institute of Materials Technology & Engineering, Chinese Academy of Sciences, Ningbo 315201, P.R. China

§ Center of Materials Science and Optoelectronics Engineering, University of Chinese Academy of Sciences, Beijing 100049, P.R. China

‡Department of Metallurgical and Materials Engineering, Indian Institute of Technology Madras, Adyar, Chennai 600036, Tamil Nadu, India

# Table of Contents



# Supplementary illustrations and explanations

**Scheme S1.** Hydrothermal synthesis reactor is used as the container to synthesize Prussian blue cubic MOF under acidic aqueous solution environment using $K_4[Fe(CN)_6]$, polyvinyl pyrrolidone (pvp).

**Figure S1.** (a,b) Rietveld refined XRD pattern and (c,d) SEM images of Prussian Blue and $Fe_2O_3$ as well as inset show their cube sizes in high magnification.

**Table S1.** Refined crystal structure parameters of Prussian blue, $Fe_2O_3$ and $Fe_2N$ at room temperature.

**Figure S2.** Low magnification of SEM image of (a-c) Prussian blue, $Fe_2O_3$ and the $Fe_2N$ that synthesized by oxidation and nitridation, (d-f) the diameter statistic histogram of Prussian blue, $Fe_2O_3$ and $Fe_2N$ cubes.

**Figure S3.** (a) The $Fe_2N$ synthesized by direct nitridation from the precursor. (b) XRD pattern of $Fe_2N$ derived from direct nitridation.

**Figure S4.** The High-resolution XPS spectra for Fe 2p of (a) Prussian Blue, (b) $Fe_2O_3$ and (c) $Fe_2N$ as well as (d) N 1s of $Fe_2N$.

**Figure S5.** The Fourier transform-infrared (FT-IR) spectroscopy patterns of (a) Prussian Blue, (b) $Fe_2O_3$ and (c) $Fe_2N$.

**Figure S6.** $N_2$ adsorption-desorption isotherms and the corresponding pore size distribution curves (inset) of Prussian blue and $Fe_2N$.

**Table S2.** Porosity details of Prussian blue and $Fe_2N$.

**Figure S7.** Photocatalytic $H_2$ evolution (a) over $Fe_2N$ with different amounts of Eosin-Y, (b) at different pH values and 80 mg of Eosin-Y for 2 h using TEOA as the

sacrificial agent and (c) comparison experiments for testing the roles of the dye and sacrificial agent. (d) Stability examination for the $Fe_2N$ sample of $H_2$ production (evacuation every 3 h).

**Figure S8**. Comparison of photocatalytic $H_2$ evolution rate between the nanoparticle and nanocubic $Fe_2N$ under optimal conditions.

**Figure S9.** Specific capacitance performances (Cyclic voltammograms) of Prussian blue, $Fe_2O_3$ and $Fe_2N$.

**Table S3.** Comparison of recently reported earth-abundant metal catalysts for photocatalytic Eosin Y-sensitized HER.

**Figure S10.** The graph for the energy band structures. The Fermi level is taken at zero.

# I. Experimental Procedures

### 1. Electrochemical measurements

The electrochemical tests are conducted on an electrochemical workstation (CHI760E, CH instrument) with a conventional three-electrode cell. A Pt plate (1cm × 1cm) is employed as the counter electrode and an Ag/AgCl (saturated) electrode was used as the reference electrode. The working electrode is prepared on a glassy carbon electrode (GCE) with a diameter of 5 mm. The exposed area of the working electrode is 0.19625 $cm^2$. The GCE is polished with $\alpha$–$Al_2O_3$ powder with decreasing sizes (1.0-0.05 μm), and it is then ultrasonically washed with deionized water and absolute ethanol before the samples were coated on it.

The electrode materials are prepared by dispersing 5 mg of the catalyst and 1 mL mixed solution, which is compounded by 25 μL of Nafion solution, 250 μL of ethanol and 750 μL of water. The mixture was then sonicated for about 1 h at room temperature to form a homogeneous ink. 10 μL of the ink (containing 0.05 mg of catalyst) was loaded onto the GCE, giving a loading mass of 0.25 mg $cm^{-2}$. The same procedure was used for all of the samples during their electrode preparation. The photocurrent measurements were carried out with the electrolyte and 0.2 M aqueous $Na_2SO_4$ solution and 0.05 M KCl solution with $K_4[Fe(CN)_6]$ and $K_3[Fe(CN)_6]$ (mole ratio 3:2). The electrochemical impedance spectroscopy (EIS) and cyclic voltammetry measurements are respectively performed in the Fe ions solution by applying an AC voltage with -1.5 mV amplitude in a frequency range from 1 Hz to 100 kHz. The bias sweep range is from -0.4 V to 0.8 V; the scanning rate of 0.1 V/s. The polarization curve is performed in the 0.2 M aqueous $Na_2SO_4$ solution with the bias sweep range from -1.6 to 0 V vs Ag/AgCl.

### 2. Computational methodology

The electronic characteristic calculations are conducted based on Density Functional Theory (DFT) implemented in quantum Espresso Package in a plane wave basis.[1] Our experimental data is used as the initial structure and the optimization is performed using Broyden, Fletcher, Goldfarb, and Shannon (BFGS) algorithm until the residual

forces are less than $10^{-4}$ eV.[2]

### 3. Turnover number (TON) and turnover frequency (TOF) calculation

For the photocatalytic water splitting, the turnover numbers (TON) are measured when the photocatalytic reaction reached the platform, while the turnover frequencies (TOF) are measured in forming a time during the reaction.

$$TON = \frac{the\ molar\ amount\ of\ gas\ production}{the\ molar\ amount\ of\ surface\ atoms\ of\ catalyst}$$

$$TOF = \frac{the\ molar\ amount\ of\ gas\ production}{the\ molar\ amount\ of\ surface\ atoms\ of\ catalyst\ \times reaction\ time\ (s)}$$

## II. Supplementary illustrations and explanations

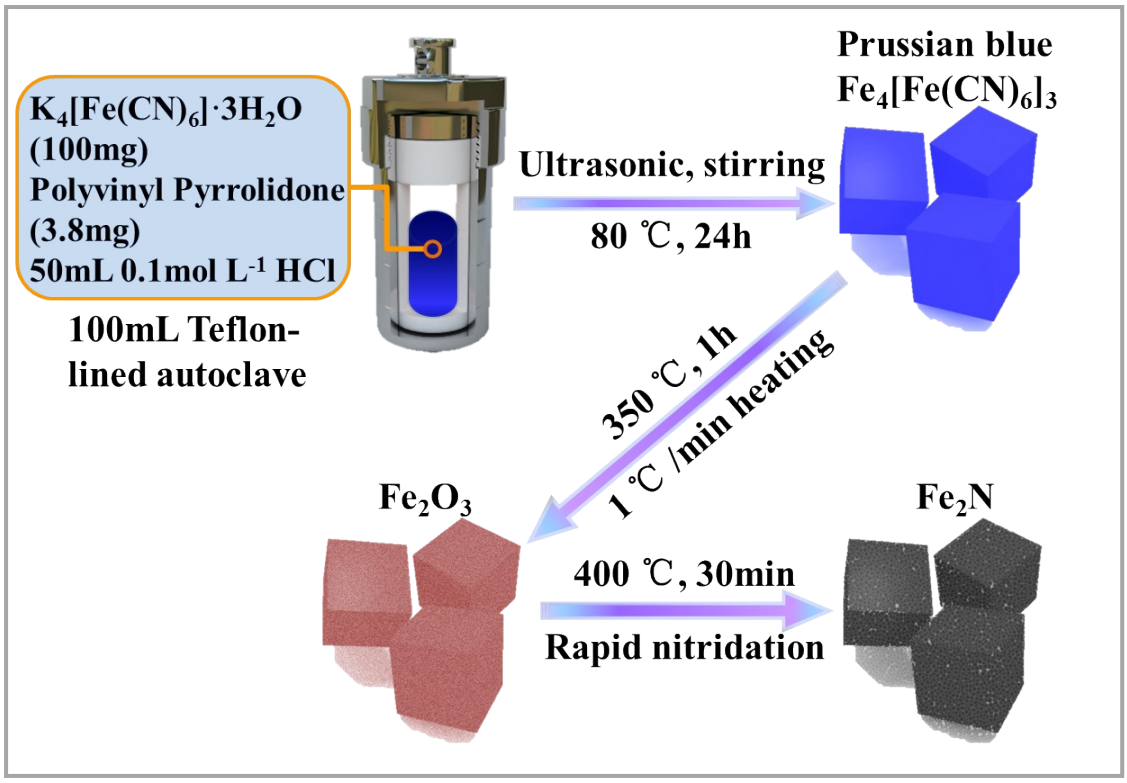


**Scheme S1.** Hydrothermal synthesis reactor is used as the container to synthesize Prussian blue cubic MOF under acidic aqueous solution environment using $K_4[Fe(CN)_6]$, polyvinyl pyrrolidone (pvp).

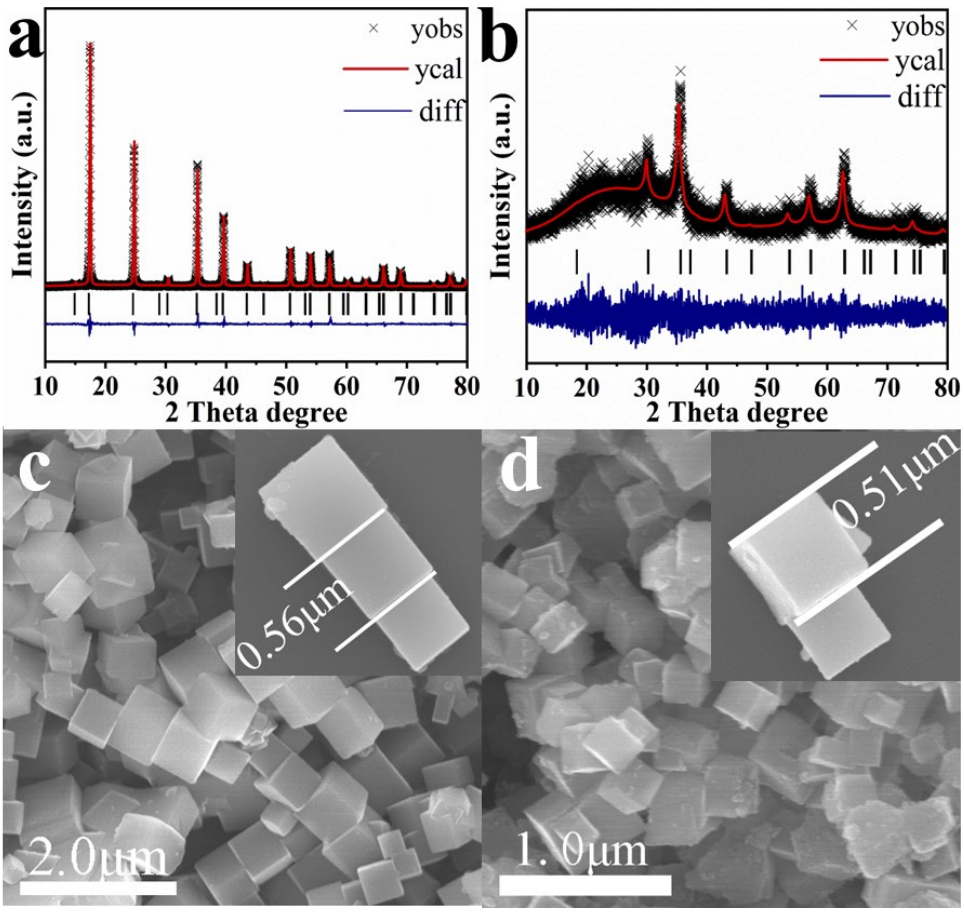


**Figure S1.** (a,b) Rietveld refined XRD pattern and (c,d) SEM images of Prussian Blue and $Fe_2O_3$ as well as inset show their cube sizes in high magnification.

**Table S1a.** Refined crystal structure parameters of Prussian blue at room temperature.

| Atom | g | x | y | z | B |
|---|---|---|---|---|---|
| **Fe1** | 0.8477 (0.0049) | 0 | 0 | 0 | 0.5 |
| **Fe2** | 1 | 0.5 | 0 | 0 | 0.5 |
| **Fe3** | 0.4519 (0.0033) | 0.25 | 0.25 | 0.25 | 21.565 (0.333) |
| **C** | 1 | 0.19440 (0.0005) | 0 | 0 | 1.266 (0.263) |
| **N** | 1 | 0.29868 (0.00041) | 0 | 0 | 3.828 (0.246) |

**Table S1b.** Refined crystal structure parameters of $Fe_2O_3$ at room temperature.

| Atom | g | x | y | z | B |
|---|---|---|---|---|---|
| **Fe1** | 0.7036 (0.0246) | 0.125 | 0.125 | 0.125 | 0.5 |
| **Fe2** | 0.6380 (0.0308) | 0.5 | 0.5 | 0.5 | 0.5 |
| **O** | 1 | 0.24372 (0.00212) | 0.24372 | 0.24372 | 1 |

**Table S1c.** Refined crystal structure parameters of $Fe_2N$ at room temperature.

| Atom | g | x | y | z | B |
|---|---|---|---|---|---|
| **Fe** | 0.9398 (0.0131) | 0.24705 (0.00082) | 0.12112 (0.00093) | 0.08379 (0.00036) | 0.5 |
| **N** | 1 | 0 | 0.37662 (0.00416) | 0.25 | 1 |

**Notes:** Numbers in parentheses are standard deviations of the last significant digit. **g**: site occupancy, **B**: isotropic thermal parameter.

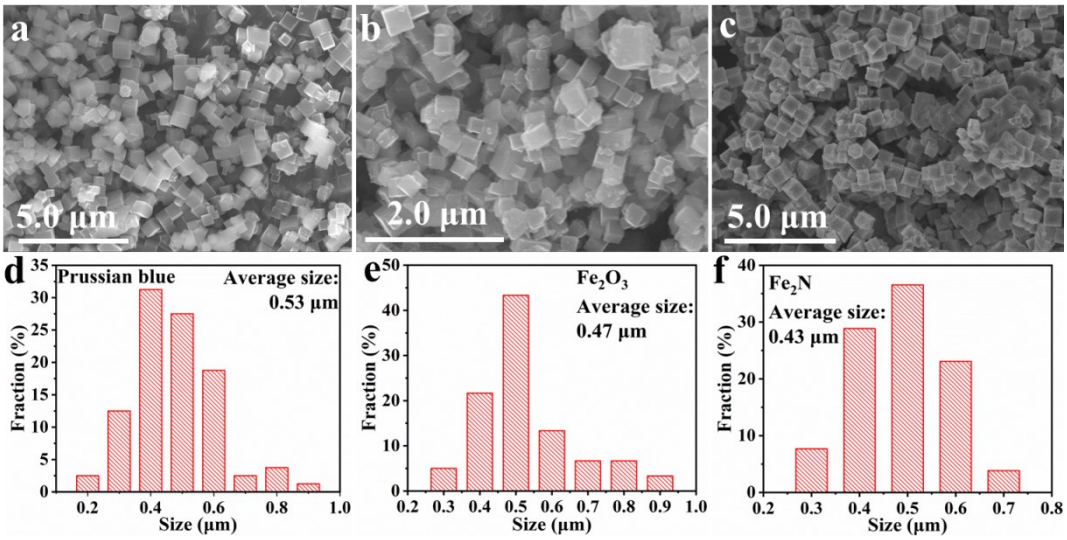


**Figure S2.** Low magnification of SEM image of (a-c) Prussian blue, $Fe_2O_3$ and the $Fe_2N$ that synthesized by oxidation and nitridation, (d-f) the diameter statistic histogram of Prussian blue, $Fe_2O_3$ and $Fe_2N$ cubes.

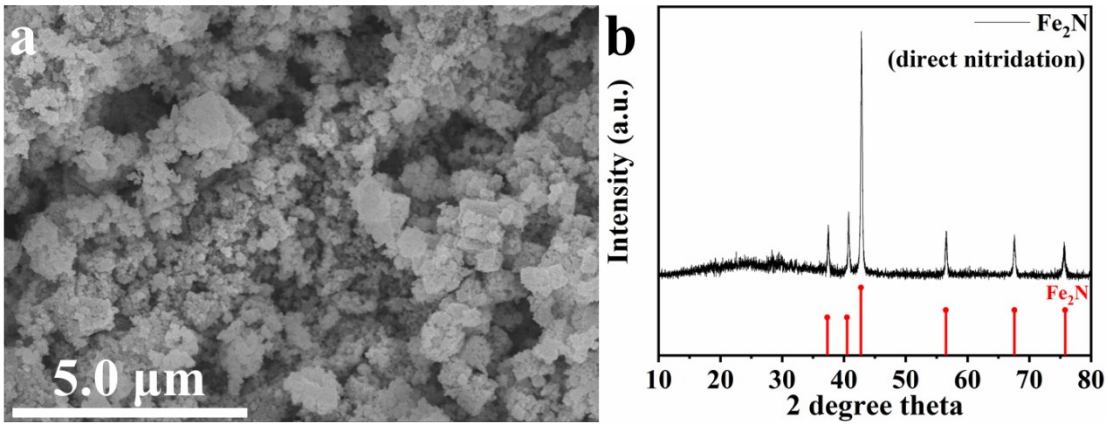


**Figure S3.** (a) The $Fe_2N$ synthesized by direct nitridation (prolong to 2 hours reaction) from the precursor. (b) XRD pattern of $Fe_2N$ derived from direct nitridation (prolong to 2 hours reaction).

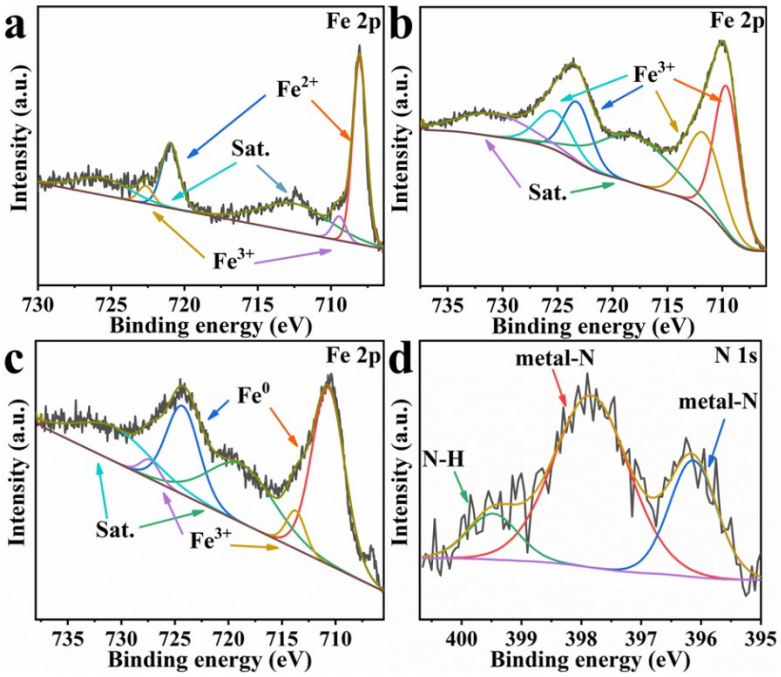


**Figure S4.** The High-resolution XPS spectra for Fe 2p of (a) Prussian Blue, (b) $Fe_2O_3$ and (c) $Fe_2N$ as well as (d) N 1s of $Fe_2N$.

**Note:** As shown in **Figure S4**, Fe 2p of Prussian Blue exhibits four main peaks at 708.05 eV ($2p_{3/2}$), 720.95 eV ($2p_{1/2}$), 709.44 eV ($2p_{3/2}$) and 722.64 eV ($2p_{1/2}$) with their satellite peaks at 712.48 eV and 725.53 eV. These peaks can be associated with the components of $Fe^{2+}$ and $Fe^{3+}$, respectively.[3-5] For sample of $Fe_2O_3$, the Fe 2p state has also shown four main peaks at 709.60 eV ($2p_{3/2}$), 723.20 eV ($2p_{1/2}$), 711.67 eV ($2p_{3/2}$) and 725.27 eV ($2p_{1/2}$), which demonstrate the existence of $Fe^{3+}$ in oxide.[6-8] The two corresponding satellite peaks are located at 718.05 eV and 730.78 eV.

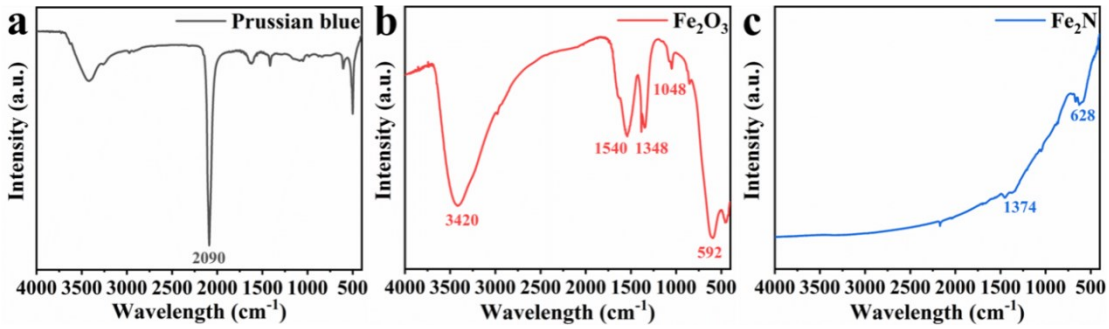


**Figure S5.** The Fourier transform-infrared (FT-IR) spectroscopy patterns of (a) Prussian Blue, (b) $Fe_2O_3$ and (c) $Fe_2N$.

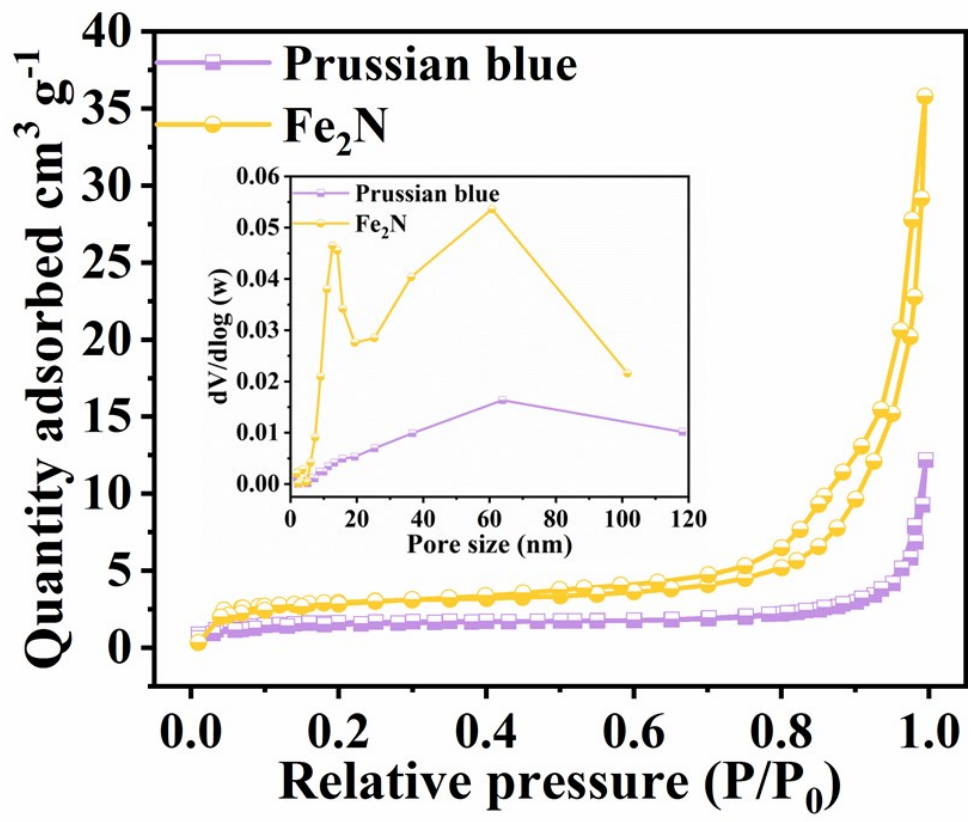


**Figure S6.** $N_2$ adsorption-desorption isotherms and the corresponding pore size distribution curves (inset) of Prussian blue and $Fe_2N$.

**Table S2.** Porosity details of Prussian blue and $Fe_2N$.

| Photocatalyst | BET surface area ($m^2\ g^{-1}$) | Mean pore size diameter (nm) | Pore volume ($cm^3\ g^{-1}$) |
|---|---|---|---|
| **Prussian blue** | 5.7357 | 36.2568 | 0.017059 |
| **$Fe_2N$** | 10.1228 | 24.7590 | 0.054475 |

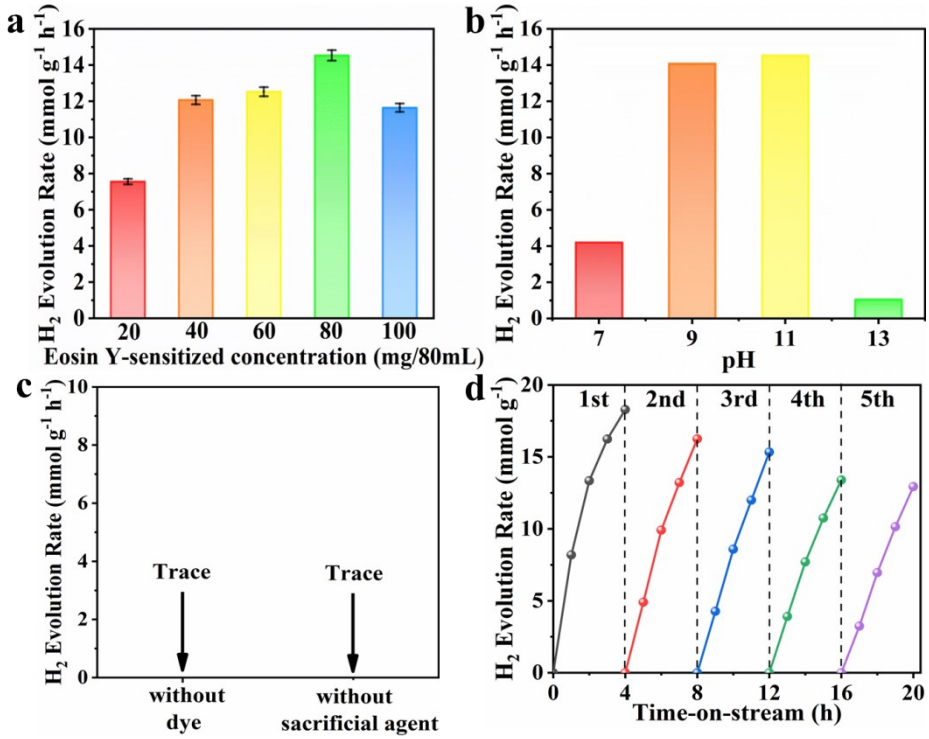


**Figure S7.** Photocatalytic $H_2$ evolution (a) over $Fe_2N$ with different amounts of Eosin-Y, (b) at different pH values and 80 mg of Eosin-Y for 2 h using TEOA as the sacrificial agent and (c) comparison experiments for testing the roles of the dye and sacrificial agent. (d) Stability examination for the $Fe_2N$ sample of $H_2$ production (evacuation every 3 h).

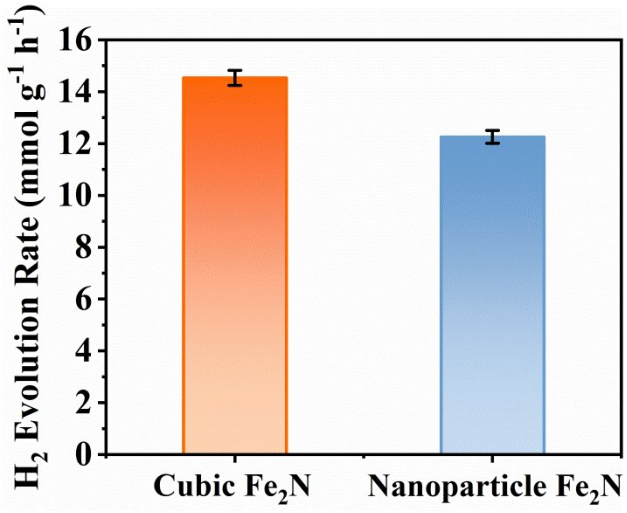


**Figure S8**. Comparison of photocatalytic $H_2$ evolution rate between the nanoparticle $Fe_2N$ and the nanocubic $Fe_2N$ under optimal conditions.

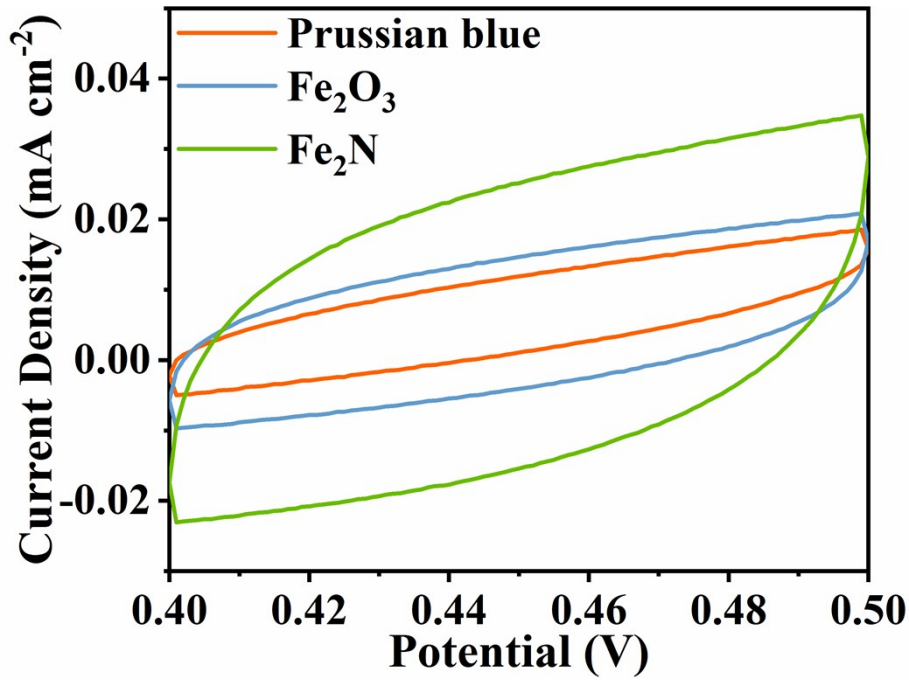


**Figure S9.** Specific capacitance performances (Cyclic voltammograms) of Prussian blue, $Fe_2O_3$ and $Fe_2N$.

**Table S3.** Comparison of recently reported earth-abundant metal catalysts for photocatalytic Eosin Y-sensitized HER.

| Catalyst | $H_2$ evolution rate (mmol $g^{-1}$ $h^{-1}$) (Cal) | pH of reactant solution | Ref. |
|---|---|---|---|
| **$Fe_2N$** | **14.5** | **10% TEOA aqueous solution (pH = 11)** | **This work** |
| Co-NCNT-800 | 14.7 | 10% TEOA aqueous solution (pH = 8.5) | R[9] |
| NP-FG | 2.74 | 10% TEOA aqueous solution (pH = 11) | R[10] |
| CoS | 1.2 | 5% TEOA aqueous solution (pH = 7) | R[11] |
| W-$Co_3S_4$ | 12.5 | 15% TEOA aqueous solution (pH = 11) | R[12] |
| NiB/GO | 6.5 | 10% TEOA aqueous solution (pH = 11) | R[13] |
| Ni@MOF-5 | 9.5 | 10% TEOA aqueous solution (pH = 11) | R[14] |
| NiP | 2.3 | 10% TEOA aqueous solution (pH = 11) | R[10] |
| $Ni(OH)_2/TiO_2$ | 1.6 | 5% TEOA aqueous solution (pH = 9) | R[15] |
| $Pt/C_3N_4$ | 0.5 | 5% TEOA aqueous solution (pH = 9) | R[16] |
| rGO/MOF/Co-Mo-S | 6.8 | 15% TEOA aqueous solution (pH = 9) | R[17] |
| Sb doped $SnO_2$ | 0.25 | 10% TEOA aqueous solution (pH = 11) | R[18] |

**Note:** The data of $H_2$ evolution rate are all calculated from the original data to the unit of **mmol $g^{-1}$ $h^{-1}$**.

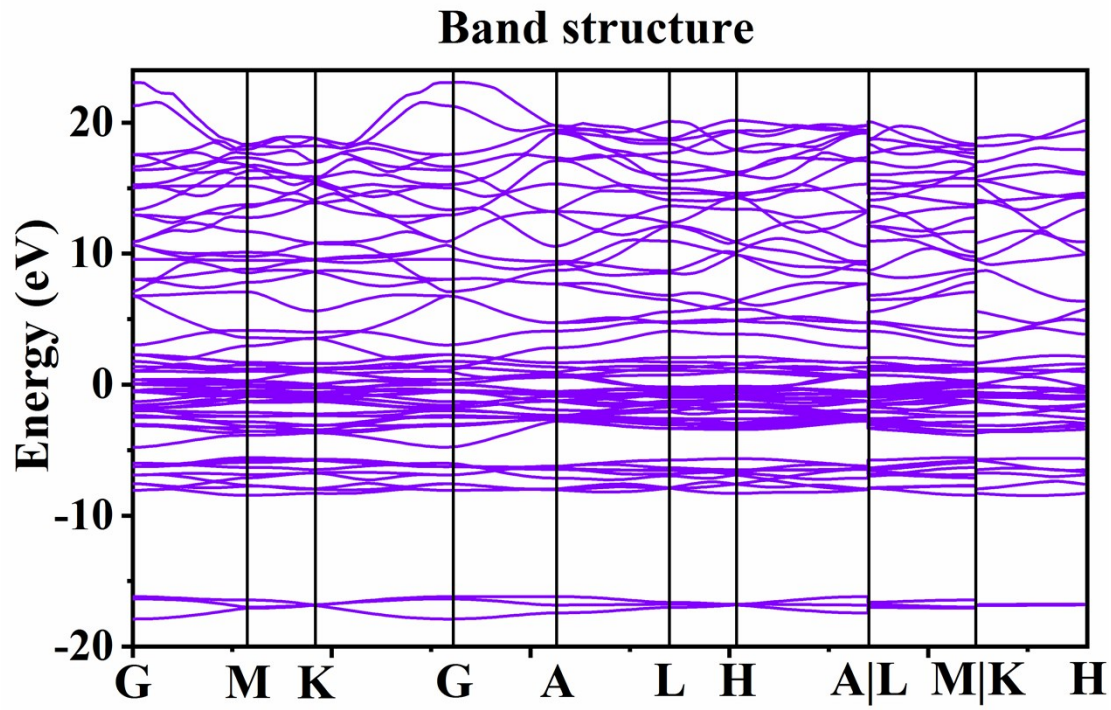


**Figure S10.** The graph for the energy band structures. The Fermi level is taken at zero.

**Note:** This figure shows that the valence band has passed through the Fermi level (zero energy) to enter the conduction band, confirming the metallicity character of the material.

## References


S1 P. Giannozzi, S. Baroni, N. Bonini, M. Calandra, R. Car, C. Cavazzoni, D. Ceresoli, G. L. Chiarotti, M. Cococcioni, I. Dabo, A. dal Corso, S. de Gironcoli, S. Fabris, G. Fratesi, R. Gebauer, U. Gerstmann, C. Gougoussis, A. Kokalj, M. Lazzeri, L. Martin-Samos, N. Marzari, F. Mauri, R. Mazzarello, S. Paolini, A. Pasquarello, L. Paulatto, C. Sbraccia, S. Scandolo, G. Sclauzero, A. P. Seitsonen, A. Smogunov, P. Umari and R. M. Wentzcovitch, *J. Phys. Condens. Matter*, 2009, **21**, 395502.

S2 J. D.Head and M. C.Zerner, *Chem. Phys. Lett.*, 1985, **122**, 264–270.

S3 M. Xia, X. Zhang, T. Liu, H. Yu, S. Chen, N. Peng, R. Zheng, J. Zhang and J. Shu, *Chem. Eng. J.*, 2020, **394**, 124923.

S4 X. W. He, L. D. Tian, M. T. Qiao, J. Z. Zhang, W. C. Geng and Q. Y. Zhang, *J. Mater. Chem. A*, 2019, **7**, 11478–11486.

S5 T. Yamashita and P. Hayes, *Appl. Surf. Sci.*, 2008, **254**, 2441–2449.

S6 J. A. R. Guivar, E. A. Sanches, F. Bruns, E. Sadrollahi, M. A. Morales, E. O. Lopez and J. Litterst, *Appl. Surf. Sci.*, 2016, **389**, 721–734.

S7 J. F. Moulder, W. F. Stickle, P. E. Sobol and K. D. Bomben, *Handbook of X-ray Photoelectron Spectroscopy, Physical Electronics*, 1992.

S8 P. Mills and J. L. Sullivan, *J. Phys. D. Appl. Phys.*, 1983, **16**, 723–732.

S9 X. Meng, Y. Dong, Q. Hu and Y. Ding, *ACS Sustain. Chem. Eng.*, 2019, **7**, 1753–1759.

S10 S. Li, N. Zhang, X. Xie, R. Luque and Y. Xu, *Angew. Chem. Int. Ed.*, 2018, **57**, 13082–13085.

S11 M. Zheng, Y. Ding, L. Yu, X. Du and Y. Zhao, *Adv. Sci. NEWS*, 2017, **27**, 1605846.

S12 H. Wang and Z. Jin, *Sustain. Energy Fuels*, 2019, **3**, 173–183.

S13 M. Yang, J. Dan, S. J. Pennycook, X. Lu, H. Zhu, Q. Xu, hong jin Fan and ghim wei Ho, *Mater. Horizons*, 2017, **4**, 885–894.

S14 W. Zhen, J. Ma and G. Lu, *Appl. Catal. B Environ.*, 2016, **190**, 12–25.

S15 Z. Yan, X. Yu, Y. Zhang, H. Jia, Z. Sun and P. Du, *Appl. Catal. B Environ.*, 2014, **160–161**, 173–178.

S16 Y. Wang, J. Hong, W. Zhang and R. Xu, *Catal. Sci. Technol.*, 2013, **3**, 1703–1711.

S17 D. Liu, Z. Jin and Y. Bi, *Catal. Sci. Technol.*, 2017, **7**, 4478–4488.

S18 L. Yang, J. Huang, L. Shi, L. Cao, W. Zhou, K. Chang, X. Meng, G. Liu, Y. Jie and J. Ye, *Nano Energy*, 2017, **36**, 331–340.